Physics of the Earth and Planetary Interiors 292 (2019) 55–66

Contents lists available at ScienceDirect

Physics of the Earth and Planetary Interiors

journal homepage: www.elsevier.com/locate/pepi

Selenophysical parameter inversion in the Lunar Southern Hemisphere Highland based on mutant particle swarm optimization

Zhen Zhong[a,b,c], Jianguo Yan[b,*], Shuanggen Jin[d,e], Menghua Zhu[f], J. Alexis P. Rodriguez[g], Huaqiang Zhu[a], Yi Li[a]

[a] School of Physics and Electronic Science, Guizhou Normal University, Guiyang 550001, China
[b] State Key Laboratory of Information Engineering in Surveying, Mapping and Remote Sensing, Wuhan 430079, China
[c] Guizhou Provincial Key Laboratory of Radio Astronomy and Data Processing, Guizhou Normal University, Guiyang 550025, China
[d] Shanghai Astronomical Observatory, Chinese Academy of Science, Shanghai 20030, China
[e] School of Remote Sensing and Geomatics Engineering, Nanjing University of Information Science and Technology, Nanjing 210044, China
[f] Space Science Institute, Macau University of Science and Technology, Avenida Wailong, Taipa, Macau, China
[g] Planetary Science Institute, 1700 East Fort Lowell Road, Suite 106, Tucson, AZ 85719-2395, USA

ARTICLE INFO

Keywords:
Particle swarm optimization
Mutation
Admittance
Elastic thickness
Lunar Southern Hemisphere highland

ABSTRACT

Selenophysical parameters can be estimated based on admittance between gravity and topography, especially high-precision GRAIL gravity and LOLA topography data. These parameters include load ratio between subsurface and surface loads, crustal thickness, crustal density, and effective elastic thickness. Considering non-negligible membrane stress, the lunar lithosphere is best modeled as a thin and elastic spherical shell. Taking into account of the nonlinearity of the governing equation of the shell and premature convergence of PSO, we introduced an updated algorithm of MPSO which considers a self-adaptive inertia weight and a mutation operator as commonly used in Genetic Algorithms (GA). Results indicate that MPSO is relatively more flexible in the choice of tuning parameters than the general algorithm of PSO. A low mutation probability of 0.005 is found to promote globally optimized convergence, and a low value of 0.002 is employed in parameters estimation for 20 areas in southern hemisphere highland. Using the updated algorithm of MPSO, it is found that a well-constrained crustal density for most of the studied regions is less than or equal to the mean crustal density (2550 $kg \cdot m^{-3}$) of the entire lunar highland. The relatively small crustal density is likely a result of high porosity of southern hemisphere crust. The elastic thickness at studied locations far from mare basins is found to be around 7 km, corresponding to the thickness at the stage of formation of highland formed from the crystallization of ancient ferroan anorthosite. A large elastic thickness is on the contrary discovered surrounding mare basins. The ancient lunar lithosphere developed quite thick as the Moon becoming cool and it was able to elastically support new loads during the formation of mare basins. The difference of elastic thickness indicates the development of lithospheric thickness at the distinct lunar evolutionary history.

1. Introduction

Selenophysical parameters inverted from gravity and topographic data provide some indicators about the internal structure and thermal evolution of the Moon (Wieczorek et al., 2013; Jin et al., 2013; Huang et al., 2014). High precision gravity data from the recent Gravity Recovery and Interior Laboratory (GRAIL) mission is now available; thus, parameters inversion based on admittance between gravity and topography is a promising alternative to other methods such those based on the limited Apollo seismic data. Moreover, the Apollo seismic stations are only located on the nearside of the Moon (Latham et al., 1973; Nakamura et al., 1973; Gillet et al., 2017), limiting the ability of traditional methods to globally constrain the lunar selenophysical parameters, especially in regions far from seismic stations. Globally distributed gravity and topographic data, especially the high precision data from recent GRAIL missions, provide an opportunity to investigate the subsurface structure of southern hemisphere highlands. Through a joint analysis of admittance between gravity and topography, it is possible to estimate selenophysical parameters based on a flexure model of either an elastic plate or spherical shell. In the case of small celestial bodies such as the Moon and Mars, modeling the lithosphere as a thin elastic spherical shell is a practical option, as the membrane

* Corresponding author.
E-mail addresses: jgyan_511@163.com, jgyan@whu.edu.cn (J. Yan).

https://doi.org/10.1016/j.pepi.2019.05.001
Received 21 June 2018; Received in revised form 24 January 2019; Accepted 1 May 2019
Available online 14 May 2019
0031-9201/

stresses' support of loads (Turcotte et al., 1981; Zhong and Zuber, 2002). Given a series of free parameters including the load ratio f, crustal thickness b_c, density ρ_c, and the lithosphere elastic thickness T_e, the resulting gravity anomalies can be inferred by solving the governing equation for the thin spherical shell. The best value of these parameters can be estimated by minimizing the misfit between the modeled admittance and observations. This method has been broadly applied in research about the Moon.

The parameter of T_e is used to describe the lithospheric thickness. It is actually considered as the effective elastic thickness, since the lithosphere is in reality not perfectly elastic (Kohlstedt et al., 1995), but we will still refer to it as the elastic thickness in the following section. The lunar lithosphere is its outer rind (Jolliff et al., 2006). Its thickness provides information about the temperature when the loadings were emplaced. On Earth, the elastic thickness is controlled by the depth of the 450 °C isotherm (Watts, 1994). A similar isotherm exists beneath the lunar lithosphere (Crosby and McKenzie, 2005). The thinner the lunar lithosphere, the smaller the elastic thickness of T_e, and therefore T_e is used to place constraints on the model of the ancient thermal evolution of a planet. Based on a thin plate model, Crosby and McKenzie (2005) first used admittance to investigate elastic thickness around the Clavius crater in the southern hemisphere of the Moon using Clementine topographic data and line-of-sight acceleration collected by the Lunar Prospector mission.

Ishihara et al. (2009) used the gravity field model SGM100g (Namiki, 2010) to study the difference of elastic thickness between the South Pole-Aitken basin (SPA) and far-side highland terrain (FHT) with the increasing precision of gravity on the farside of the moon. Later, Huang and Wieczorek (2012) used SGM100i (Goossens et al., 2011) to estimate the density and porosity of the whole upper crust. The gravity field model SGM100g was a prior model used in an iteration process to obtain SGM100h (Matsumoto et al., 2010). This model was solved not only using the Doppler tracking data of SELENE mission (from 20 October 2007 to 26 December 2008 plus 30 January 2009), including two-way Doppler tracking data of the main orbiter, and all the four-way tracking data, but also considering other historical tracking data from the LP, Clementine, and the Apollo sub-satellite. As the additional same-beam differential VLBI tracking data between Rsta and Vsta of SELENE mission became available, Goossens et al. (2011) combined these VLBI data and those used to solve SGM100h to obtain a new model, SGM100i. This new model showed an improvement in orbit determination over the previous SGM100g and SGM100h models.

It is now possible to study small-scale areas with the unprecedentedly high precision of the GRAIL gravity field model now available. Huang et al. (2014) first employed GRAIL gravity field model and topographic data from LOLA to estimate T_e over large volcanic complexes on the nearside of the Moon. Their research revealed a quite lower T_e on the nearside (even close to 1 km). Analogously, Zhong et al. (2014) first considered a Particle Swarm Optimization (PSO) in admittance inversion. They applied such algorithm to T_e inversion over the Grimaldi mare basin and found a low value of 30 km (Zhong et al., 2017). Their result is quite lower than the previous value (~60 km) (Arkani-Hamed, 1998; Sugano and Heki, 2004). These researches reveal that the elastic thickness from GRAIL gravity field model is likely lower than models from non-GRAIL data.

The low-precision non-GRAIL gravity field models have been less extensively employed on southern lunar highlands with limited inversion. Although Crosby and McKenzie (2005) studied parts of these places, the lithosphere they modeled was a thin plate. The lithosphere is best modeled however, as a thin spherical shell, considering the non-negligible membrane stresses' support to loads. Combining the thin spherical shell model with the high-precision GRAIL gravity data makes possible new insights into the substructure beneath the southern highland. Moreover, the primordial topography on the southern highland was formed during the crystallization of ancient ferroan anorthosite. Investigation on the elastic thickness in the southern highlands can provide information about the strength of the lithosphere when it started to grow. High-precision GRAIL gravity field models and topography data from LOLA make it possible to carry out extensive inversion. So far, there is no such similar research on the lunar southern highlands, since it was difficult to make an extensive inversion on this area using the low-precision non-GRAIL gravity field.

Considering the nonlinear nature of the governing equation of the spherical shell (see Eq. (C1) in Appendix), solving such an equation is complex when using traditional linearized approaches to estimate parameters based on statistical admittance. Moreover, these linearized methods will face more computational challenge when executing an inversion. From a theoretical point of view, nonlinear global optimization methods that synchronously sample all the parameters in wide ranges are the optimal strategy. To solve these problems, the Monte Carlo (MC) and Markov Chain Monte Carlo (MCMC) methods were introduced as global optimization methods in selenophysics (Khan et al., 2000; Chenet et al., 2006; Huang and Wieczorek, 2012; Huang et al., 2014; Matsumoto et al., 2015). These approaches can be applied on non-smooth and non-convex object functions, since they are derivative-free and generate results independent of an initial model; however, they are extremely time-consuming methods.

Evolutionary algorithms (EA) have experienced rapid development, particularly as they are efficient at global optimization with high rates of convergence. One of the powerful EA methods is Particle Swarm Optimization (PSO), known for simplicity of implementation and few tuning parameters (Kennedy and Eberhart, 1995). It performs effectively in selenophysical parameter inversion (Zhong et al., 2014, 2017). However, like other EA methods such as Genetic Algorithm (GA), PSO is also prone to premature convergence, especially in functions with complex shapes (Taherkhani and Safabakhsh, 2016). Premature convergence means inversion failure, since particles merely find localized values for these estimated parameters. Thus, the key issue is how to escape from localized solutions. Inspired by the mutation operator employed in Genetic Algorithm (GA) (Ali et al., 2016), we introduced an updated version of PSO with a mutation operator and a self-adaptive inertia weight, Mutant Particle Swarm Optimization (MPSO), that avoids premature convergence.

In this paper, we adopt our algorithm to study the lithospherical thickness information in the lunar southern highland areas; especially we demonstrate the superior robustness of MPSO over the general PSO. Perfect MPSO convergence rates will ensure its successful application in selonophysical parameter inversion on the lunar southern hemisphere highland, as well as its potential application in geophysical parameter inversion for Mars' and Venus'. We organize the paper as follows: we introduce the proposed method in Section 2; we demonstrate the advantage of MPSO over PSO with a sensitivity analysis in Section 3; in Section 4, we present the results and discussion; and finally, we summarize our work and draw conclusions in Section 5.

2. Theory and methods

2.1. Particle swarm optimization

The PSO was originally introduced by Kennedy and Eberhart (1995) to simulate social behaviors found in flocks of birds or schools of fish, especially their movements. It creates a swarm of candidate solutions

represented as particles. All the particles move around in a search-space composed by the ranges of estimated parameters. For the admittance analysis in this paper, there are four parameters to be estimated. These include the load ratio f, crustal thickness b_c, density ρ_c, and lithosphere elastic thickness T_e. Thus, the corresponding search space is four dimensions. The i-th particle of the swarm is represented by a 4-dimensional position vector $x_i = (f_i, b_{c,i}, \rho_{c,i}, T_{e,i})$, where f_i, $b_{c,i}$, $\rho_{c,i}$ and $T_{e,i}$ are the candidate solutions for the estimated parameters. The velocity is $v_i = (v_{i1}, v_{i2}, v_{i3}, v_{i4})$. If we use t as an iteration index, then the current position and velocity of the i-th particle are represented by $x_i(t)$ and $v_i(t)$, and the best position ($P_{i,\mathrm{best}}$) from the beginning to current iteration t is $P_{i,\mathrm{best}} = (f_{i,p}, b_{c,i,p}, \rho_{c,i,p}, T_{e,i,p})$. The current global best position ($P_{g,\mathrm{best}}$) for all the particles is $P_{g,\mathrm{best}} = (f_g, b_{c,g}, \rho_{c,g}, T_{e,g})$. The velocity and position of the i-th particle at the next iteration $t + 1$ can be calculated by the following equations (Kennedy and Eberhart, 1995; Kennedy et al., 2001);

$$v_i(t+1) = \omega v_i(t) + c_1 r_1[p_{i,\mathrm{best}} - x_i(t)] + c_2 r_2[p_{g,\mathrm{best}} - x_i(t)] \quad (1)$$

$$x_i(t+1) = x_i(t) + v_i(t+1) \quad (2)$$

in which, c_1 and c_2 are cognitive and social parameters, r_1 and r_2 are uniform random numbers between 0 and 1, and ω is the inertia weight, showing the effect of a previous velocity vector on the new vector.

2.2. Self-adaptive inertia weight and mutation operator

The inertia weight ω in PSO adjusts the influence of a previous velocity on the current velocity and makes a balance between global and local exploration (Shi and Eberhart, 1998). In general, a large inertia weight permits a powerfully global exploration, promoting particles to escape from local solutions. A small inertia weight value will tend toward local exploration, confining particle searches within its nearby ranges and thus promoting convergence. It is more rational therefore, that the inertia weight ω varies asynchronously according to potential solutions. This strategy is called the self-adaptive inertia weight and has been demonstrated to be quite effective (Taherkhani and Safabakhsh, 2016). The inertia weight of the i-th particle at the iteration t can be estimated as follows:

$$\omega_i = \begin{cases} \omega_{\min} - \dfrac{(\omega_{\max} - \omega_{\min})\cdot(\sigma_i - \sigma_{\min})}{\sigma_{avg} - \sigma_{\min}} & (\sigma_i \le \sigma_{avg}) \\ \omega_{\max} & (\sigma_i > \sigma_{avg}) \end{cases} \quad (3)$$

where $\omega_{\max}$ and $\omega_{\min}$ represent the maximum and minimum values of the inertia weight, respectively, σ_i is misfit value for the i-th particle at the last iteration t-1, $\sigma_{\min}$ and σ_{avg} represent the minimum and mean values of the misfit function of a swarm, respectively.

The strategy of self-adaptive inertia weight can suffer from premature convergence when the objective function is great complex; so another effective method is needed. Mutation in Genetic Algorithm (GA) is a genetic operator used to maintain genetic diversity. Given a user-definable mutation probability, it will alter one or more gene values in a chromosome (Dai et al., 2006) from their initial states. In the MPSO, a particle and its position correspond to a chromosome and gene in GA, respectively. A mutation operator in the MPSO will randomly alter one component of the position vector for an arbitrary particle. This operator allows the algorithm to avoid a local best solution by preventing the particles from becoming too similar to each other. In this paper, we insert the mutation operator after Eq. (2), which implies a mutation operating in the swarm after each particle is updated for velocity and position. The flowchart of the MPSO algorithm is described in Appendix A.

2.3. Admittance between gravity and topography

The gravity g and topography h on a reference sphere can be expressed by a linear combination of spherical harmonics as in (Wieczorek and Simons, 2005, 2007)

$$g(\Omega) = \sum_{lm} g_{lm} Y_{lm}(\Omega),\ h(\Omega) = \sum_{lm} h_{lm} Y_{lm}(\Omega) \quad (4)$$

where Y_{lm} is a spherical harmonic of degree l and order m, g_{lm} and h_{lm} represent the spherical harmonic expansion coefficients of g and h, respectively, Ω represents a position on the sphere in terms of colatitude θ and longitude ϕ. In order to investigate the selenophysical parameters in a localized area within an angular radius θ_0, the global distributed gravity and topography must be localized by an axisymmetric windowing function $\psi(\theta_0)$ up to maximum degree l_{win} (Wieczorek and Simons, 2005, 2007)

$$\psi(\theta_0) = \sum_{j=0}^{l_{win}} \psi_j \overline{P}_j(\cos\theta_0) \quad (5)$$

where $\overline{P}_j(\cos\theta_0)$ is the normalized Legendre's polynomial of degree j. This function is constructed to minimize signals arising from areas exterior to the angular radius θ_0 for the given spectral bandwidth l_{win}. We use a single localization window that can concentrate more than 99% of its power within the region of interest. The localized gravity and topography are $g(\Omega)\psi(\theta_0)$ and $h(\Omega)\psi(\theta_0)$, respectively. We assume that Φ_{lm} and Γ_{lm} are the spherical harmonic expansion coefficients of the localized gravity and topography, respectively. The total cross-power $S_{\Phi\Gamma}(l)$ of the localized gravity and topography is defined as

$$\sum_{l=0}^{\infty} S_{\Phi\Gamma}(l) = \sum_{l=0}^{\infty}\sum_{m=-l}^{l} \Phi_{lm}\Gamma_{lm} = \frac{1}{4\pi}\int_{\Omega}[\psi(\theta_0)g(\Omega)][\psi(\theta_0)h(\Omega)]d\Omega \quad (6)$$

Similarly, we can get the auto-power spectrum $S_{\Phi\Phi}(l)$ and $S_{\Gamma\Gamma}(l)$ of the localized gravity and topography. Thus, the wavelength-dependent localized admittance $z(l)$ and correlation $\gamma(l)$ can be given by.

$$z(l) = \frac{S_{\Phi\Gamma}(l)}{S_{\Gamma\Gamma}(l)},\ \gamma(l) = \frac{S_{\Phi\Gamma}(l)}{\sqrt{S_{\Phi\Phi}(l)\cdot S_{\Gamma\Gamma}(l)}} \quad (7)$$

The localized admittance error squared can then be estimated as in (Bendat and Piersol, 2000; Wieczorek and Simons, 2007),

$$\sigma_z^2(l) = \frac{S_{\Gamma\Gamma}(l)}{S_{\Phi\Phi}(l)}\frac{1-\gamma^2(l)}{2l} \quad (8)$$

2.4. Misfit function and governing equation of a spherical shell

Given a serial of parameters such as ρ_c, f, b_c and T_e, the modeled gravity is deduced from the governing equation of thin spherical shell. Using Eqs. (4)–(7), we can calculate the modeled admittance. If gravity and topography are correlated, the four parameters can be estimated by minimizing the misfit between the modeled admittance and observations (Belleguic et al., 2005; Beuthe et al., 2012). The misfit is denoted by the chi-squared function (Belleguic et al., 2005; Beuthe et al., 2012)

Table 1
Nominal parameter values.

Parameter name	Value or range
Load ratio f	−0.8–5
Mean crustal density ρ_c (kg·m^{-3})	2000–3200
Mean crustal thickness b_c (km)	0.0–60
Lithospheric elastic thickness T_e (km)	0.0–150
Surface gravity acceleration g (m·s^{-2})	1.721
Referenced radius R (km)	1737.15
Poisson's ratio of lithosphere ν	0.25
Young's modulus of lithosphere E (Pa)	1.0×10^{11} (McGovern et al., 2002)
Mantle density ρ_m (kg·m^{-3})	3360 (Garcia and Gagnepain-Beyneix, 2011)

$$\sigma^2 = \frac{1}{N}\sum_{l=l_{win}}^{l_{max}}\left[\frac{z^{obs}(l) - z^{mod}(l)}{\sigma_z(l)}\right]^2 \quad (9)$$

where $z^{obs}(l)$ and $z^{mod}(l)$ are the observed and modeled admittances for a given degree l in terms of Eq. (7), $\sigma_z(l)$ is the error of the observed admittance shown in Eq. (8). The value l_{win} is the maximum degree of the windowing function as shown in Eq. (5), while l_{max} is the maximum degree of utilized gravity field model. N is the number of degrees of freedom (here equals l_{max}-2l_{win}-4 in this study). The standard deviation of the chi-squared function is approximately equal to $\sqrt{2/N}$. The global best-values of the parameters can be constrained within $2\sigma_{STD} = 2\sqrt{2/N}$.

The modeled admittance $z^{mod}(l)$ can be estimated based on the modeled gravity anomaly contributed by the surface topography and subsurface interfaces. These interfaces depend on the deflection w_L of the lithosphere and their relieves are shown in Table C1. Given a certain load q (positive downward), the deflection w_L of a thin and elastic shell is governed by the following expression (Kraus, 1967; Turcotte et al., 1981)

$$D\nabla^6 w_L + 4D\nabla^4 w_L + ET_eR^2\nabla^2 w_L + 2ET_eR^2 w_L = R^4[(\nabla^2 + 2) - (1 + \nu)]q \quad (10)$$

where R is the reference radius of the shell (equivalent to the lunar mean radius) and E is Yong's modulus. ν is Poisson's ratio and $D = ET_e^3/[12(1\text{-}\nu^2)]$ is the flexural rigidity (as shown in Table 1). Eq. (10) is characterized by nonlinearity with a high order of six, and thus can be solved with a nonlinear rather than linear method.

3. Sensitivity analysis

In order to test the advantage of MPSO, we analyzed the success rate (SR) distribution considering just the mutation operator, without the self-adaptive inertia weight. This factor SR will approach 100% when the MPSO finds the global best minimum for the testing function Rastrgin (As seen in Table B1). It is also a function of variable tuning parameters such as inertia weight ω, cognitive and social parameters c_1 and c_2. We set the inertia weight ω varying in the range [0, 1]. We also suppose parameters c_1 and c_2 identical to each other ($c_1 = c_2 = c$), as is in general recommended in the literature (Shi and Eberhart, 1998), and constrain their value c varying in the range [0, 3]. The number of iterations is 100 in our test. For every couple of parameters (ω, c), we take 100 trials to analyze the sensitivities for the swarm sizes $n = 20$ and $n = 60$. As shown in Fig. 1(a) and (b), the SR for both PSO and MPSO is sensitive for tuning parameters ω and c for a small swarm size $n = 20$. In this case, the optimal ω is dependent on c, but the area of SR in MPSO is larger than that of PSO.

As the size n increased to 60 as in Fig. 1(c) and (d), the area of SR for

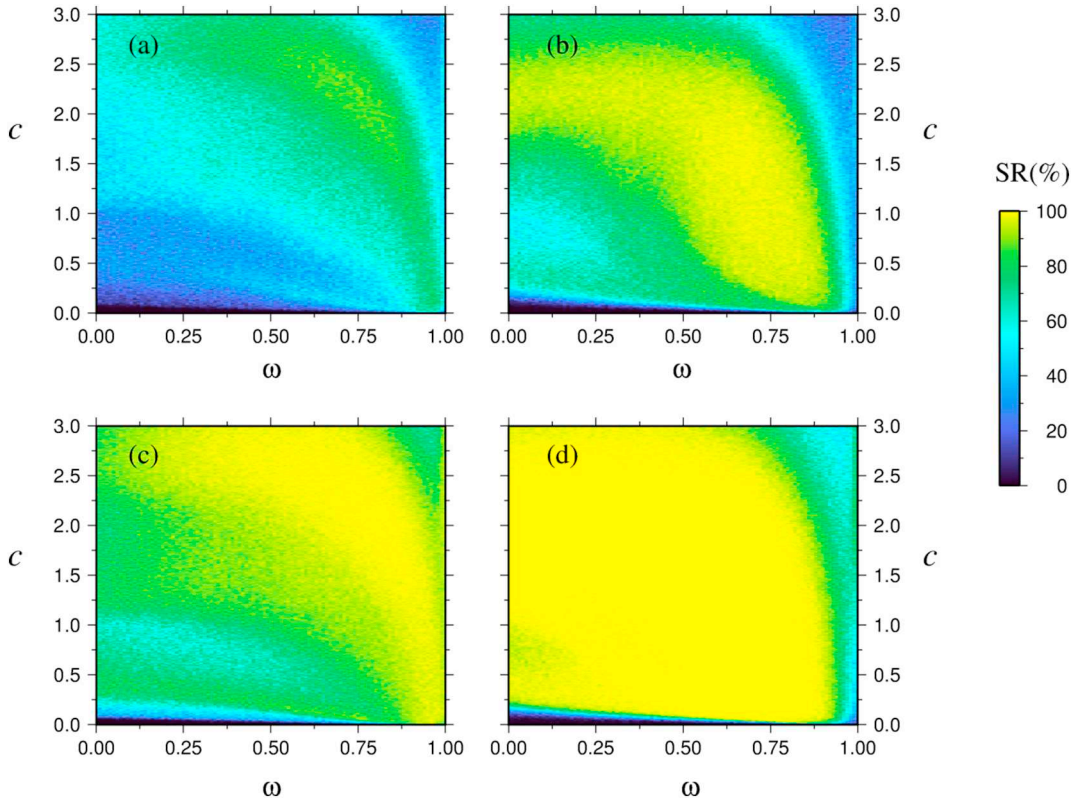

Fig. 1. SR as a function of variable tuning parameters ω and c. For PSO, the swarm sizes have different value of $n = 20$ and $n = 60$ in (a) and (c), respectively. As to MPSO, the swarms sizes are $n = 20$ and $n = 60$ in (b) and (d), respectively.

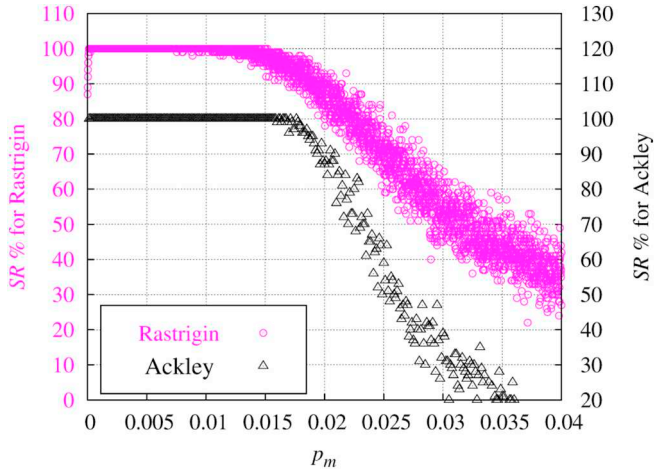

Fig. 2. Sensitivity analysis for mutation probability p_m for two multimodal functions of Rastrigin and Ackley.

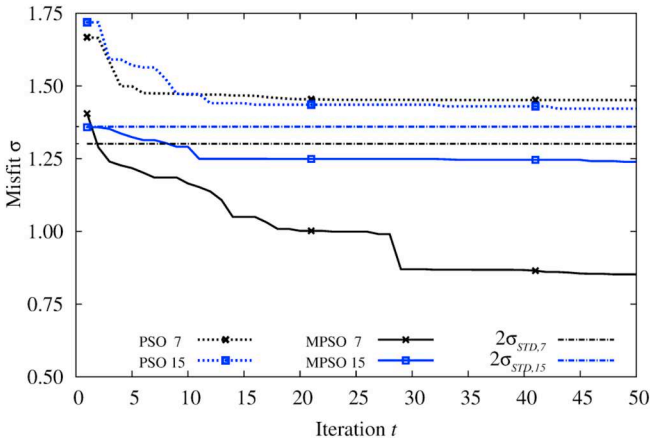

Fig. 3. Differences of convergence between PSO (dashed lines) and MPSO (solid lines). No. 7 and No. 15 represent areas centering at (50°S, 9°E) and (55°S, 51°E) in Table 2, respectively. The two-standard deviations for No. 7 ($2\sigma_{STD,7}$) and No. 15 ($2\sigma_{STD,15}$) are represented by dashed lines with black and blue colors, respectively. (For interpretation of the references to color in this figure legend, the reader is referred to the web version of this article.)

both PSO and MPSO becomes larger than those of the corresponding small size swarm $n = 20$. However, the area of SR for MPSO is much larger than that of PSO in this situation. This result coincides with the result for a small swarm size $n = 20$, indicating the mutation operator is an effective way to avoid local minimums. If the swarm size n increases to a larger number such as $n = 400$, we can infer that the SR region will be wider. It is evident that the range of the optimal ω in MPSO is wider than that of PSO for a given c. This result reveals that there is more independency between ω and c for MPSO than in PSO. Therefore, MPSO is more flexible than PSO when selecting ω and c. Based on the large value of SR in Fig. 1, we selected $c = 2.0$, $\omega_{max} = 0.8$, and $\omega_{min} = 0.3$ in our study.

The sensitivity of mutation probability p_m in MPSO was tested, considering the self-adaptive inertia weight and mutation operator. The test aimed to identify the optimum range for the mutation probability for parameters estimation. The Rastrigin and Ackley multimodal functions were employed in our experiment as these n dimensional functions are non-linear and large number of local minima to test the robustness of an algorithm. These functions are detailed in Appendix B. In Fig. 2, the two functions show the same SR value (~100%) at a low mutation probability. This low probability falls in the range of (0, 0.01). Beyond this range, the success rates drop slowly, which means that a large mutation probability will likely lead to a low success rate. Considering that, a mutation operator will reset the position of a target particle, and a large probability means a large number of particles shift

Table 2
Summary of inversion parameters. θ_0 is the angular radius, l_{max} is the maximum degree of utilized gravity and topography data, f is the load ratio between subsurface and surface loads, b_c is the crustal thickness, ρ_c is the crustal density, T_e is elastic thickness and σ is the misfit.

No.	Center	θ_0	l_{max}	f	b_c (km)	ρ_c (kg·m^{-3})	T_e (km)	σ
1	(33°S, 42°W)	5	170	$3.448_{-0.738}^{+0.228}$	41.5_{-15}^{+12}	2950_{-136}^{+73}	40_{-10}^{+10}	1.0861
2	(42°S, 31.5°W)	5	170	−0.2859	23.4	2340.5	20.2	1.6666
3	(50°S, 35°W)	5	200	−0.5386	28.0	2200.0	28.8	1.5332
4	(42°S, 15°W)	5	170	$0.38_{-0.026}^{+0.023}$	$38_{-1.7}^{+2.3}$	2485_{-8}^{+13}	30_{-28}^{+15}	0.9579
5	(41°S, 2°W)	5	170	−0.0429	30	2666.2	9.9	1.6525
6	(42°S, 8°E)	7	200	$-0.35_{-0.027}^{+0.017}$	$28_{-1.2}^{+2.0}$	2400_{-15}^{+12}	8_{-3}^{+6}	0.9933
7	(50°S, 9°E)	5	200	$-0.17_{-0.042}^{+0.047}$	33_{-5}^{+9}	2550_{-22}^{+17}	$6_{-1.65}^{+3.18}$	0.7284
8	(37°S, 25°E)	5	170	0.2090	30.0	2720.2	4.5	2.0211
9	(46°S, 25°E)	5	170	0.4374	28.0	2808.5	19.2	1.5184
10	(58°S, 25°E)	7	200	0.0982	28.0	2547.2	3.3	1.3239
11	(35°S, 36°E)	6	170	$-0.43_{-0.030}^{+0.034}$	$30_{-3.2}^{+3.5}$	2280_{-28}^{+23}	12_{-5}^{+101}	0.7678
12	(53°S, 36°E)	5	200	−0.2607	30.0	2400.0	27.2	2.1588
13	(63°S, 39°E)	8	170	−0.2433	32.5	2518.2	2.6	1.9669
14	(35°S, 47°E)	5	170	$-0.354_{-0.003}^{+0.003}$	$35.2_{-0.3}^{+0.3}$	2400_{-4}^{+1}	13_{-1}^{+2}	1.3586
15	(55°S, 51°E)	6	170	$-0.355_{-0.0034}^{+0.0044}$	$26_{-1.3}^{+1.1}$	2450_{-6}^{+5}	$3.0_{-0.34}^{+0.46}$	1.2389
16	(50°S, 70°E)	5	200	$-0.36_{-0.030}^{+0.035}$	$35_{-1.5}^{+2.8}$	2342_{-18}^{+10}	12_{-3}^{+6}	1.2421
17	(45°S, 65°E)	6	170	−0.2505	25.0	2501.3	4.1	1.6610
18	(35°S, 75°E)	6	170	−0.1479	33.5	2418.9	10.2	1.9037
19	(28°S, 87°E)	8	170	−0.2934	36.7	2485.5	2.6	1.6183
20	(35°S, 85°E)	5	170	$-0.273_{-0.005}^{+0.005}$	$24_{-3.5}^{+4.5}$	2570_{-7}^{+11}	$2.4_{-0.16}^{+0.18}$	0.6924

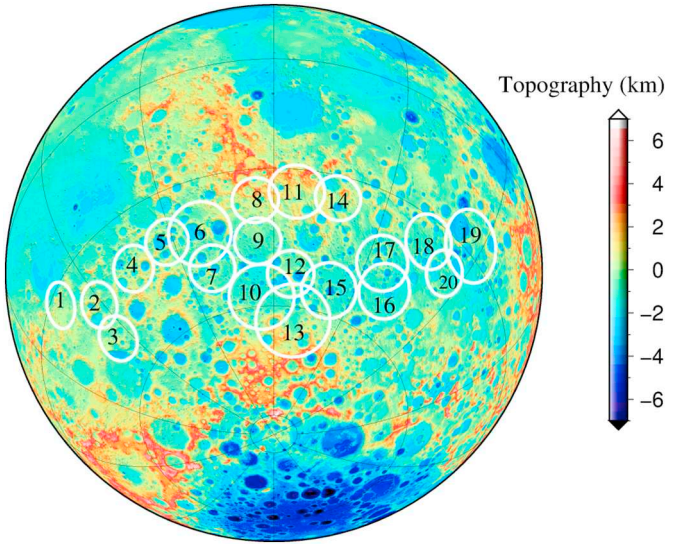

Fig. 4. Hemisphere map centering at (35°S, 30°E) using the Lambert azimuthal equal-area projection comes from LOLA topography. Studied areas with a number of tags from 1 to 20 are circled with white color.

toward a primitive random search. Therefore, this probability ought to be set as a low value; a value around 0.005 is suggested by Fig. 2. A low value of 0.002 was applied in our study.

4. Selenophysical parameter estimation

The high-resolution gravity field model GL0660B (Konopliv et al., 2013) and LOLA topography data (Smith et al., 2010) were used in our analysis. GL0660B was expanded to degree and order 660, it is an update of the preliminary lunar gravity field model GL0420A (Zuber et al., 2013), and has 98% global coherence with the LOLA topography to a degree of 330. Considering that the deflection of the lunar crust-mantle interface in response to surface loads makes only a negligible contribution to the observed gravity field beyond degree and order 150 (Wieczorek et al., 2013), the gravity and topography data were conservatively truncated up to 170 or 200 (corresponding to maximum degree l_{max} = 170 or 200). The admittance computation between gravity and topography was carried out using the SHTOOLS2.8 archive (Wieczorek and Meschede, 2018). The actual lithospherical deflection possibly resulted from surface and subsurface loads; these loads were also considered. Given a series of estimated parameters, the gravity anomaly was estimated according to Appendix C. All the parameters values or ranges are listed in Table 1. In general, a large angular radius θ_0 includes more waves, but leads to a lower resolution. In order to make a trade-off between the resolution and success of estimation, the areas of interested were confined within an angular radius from 5° to 8°, corresponding to a spherical harmonic bandwidth of 52 or 32. These angular radii contain most of the localized gravity anomalies. For an angular radius of 5° and maximum degree l_{max} = 170, the corresponding effective degrees used in our analysis ranged from 52 to 148, with a degree of freedom of 61. Similarly, using the same angular radii but when considered as a large maximum degree l_{max} = 200, the degree of freedom will be 91.

We made a comparison between PSO and MPSO to test the convergence speed. We selected two areas (i.e. No. 7 and No. 15 in Fig. 4) in our test. These two areas were constrained within $2\sigma_{STD}$, as presented in Table 2. The center positions of these areas were located at (50°S, 9°E) and (55°S, 51°E). The results are shown in Fig. 3. The swarm size was 400 and number of iterations was less than 50. In area No. 7, the misfit σ declined rapidly before iteration 20. However, the misfit σ for MPSO was confined within $2\sigma_{STD}$ (~0.3015), but was greater than $2\sigma_{STD}$ in PSO. When constrained within $2\sigma_{STD}$ (~0.3203), MPSO shows the same behavior of convergence in other areas of No. 15, but PSO exhibits divergence within 50 iterations, thus MPSO has more powerful capacity of convergence than PSO. This indicates that the mutation factor and self-adaptive inertia weight included in MPSO speeds up convergence. These strategies can help particles escape from local minimization solutions.

We inversed the parameters for 20 areas on the highland of lunar southern hemisphere by applying swarm sizes of 400 with 50 iterations. The misfit for most of these areas was constrained within two-standard deviations; these 20 areas represent most of the features in the southern highland. Using the Lambert azimuthal equal-area projection, these areas were plotted on a hemisphere map circled with black color in Fig. 4. We selected two areas to illustrate their best-fit admittance, as seen in Fig. 5; panels (a-b) represent admittances for areas of No. 7 and No. 15. Constrained within $2\sigma_{STD}$ (~0.3015), Fig. 5a shows that the admittance in No. 7 had a sharp upturning profile until degree 67. After degree 67, the admittance appears as an approximate straight line, with little fluctuation. The correlation spectrum gets close to unity across the whole range. It is clear that the misfit between the modeled admittance (pink solid line) and observed admittance (black error bar) is quite small except for four points at the beginning of spectrum. This best fit also applies in No. 15, shown in Fig. 5b, except for misfits at few points. These results indicate a significant advantage of MPSO when searching for global optima. The optimal estimated parameters for the area of No.

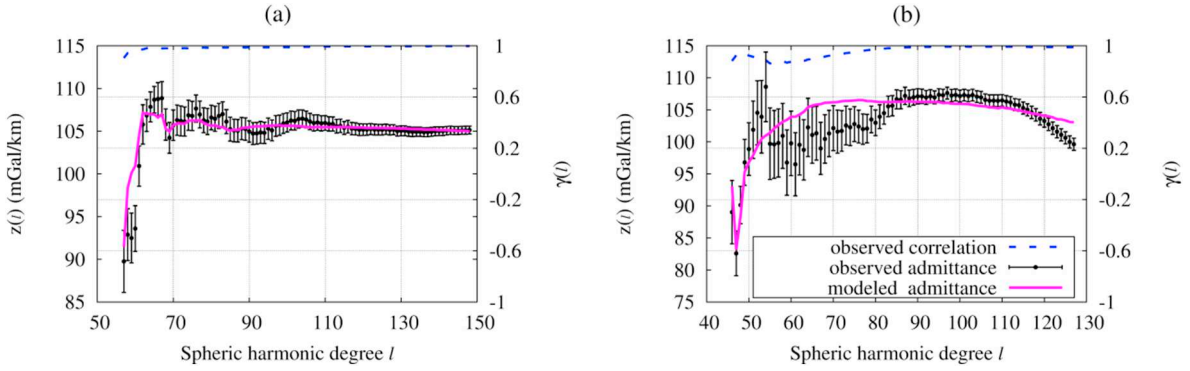

Fig. 5. Correlation spectrum observed (dashed line), admittance spectrum observed (error bar) and admittance spectrum modeled (solid line) for two regions. (a) denotes region of No. 7 and (b) designates regions of No. 15 in Fig. 4 and Table 2.

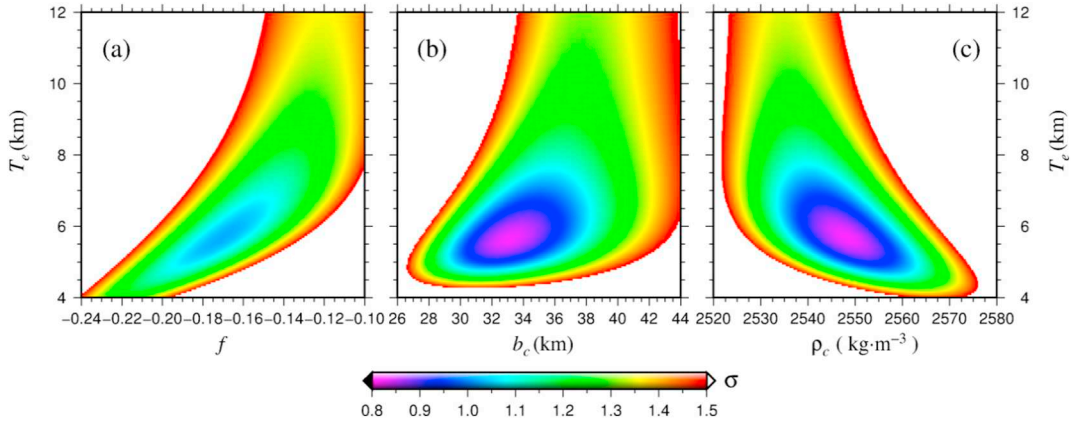

Fig. 6. RMS misfits σ in the trade-off studies between (a) f vs. T_e, (b) b_c vs. T_e and (b) ρ_c vs. T_e for area No. 7 in Fig. 4 and in Table 2.

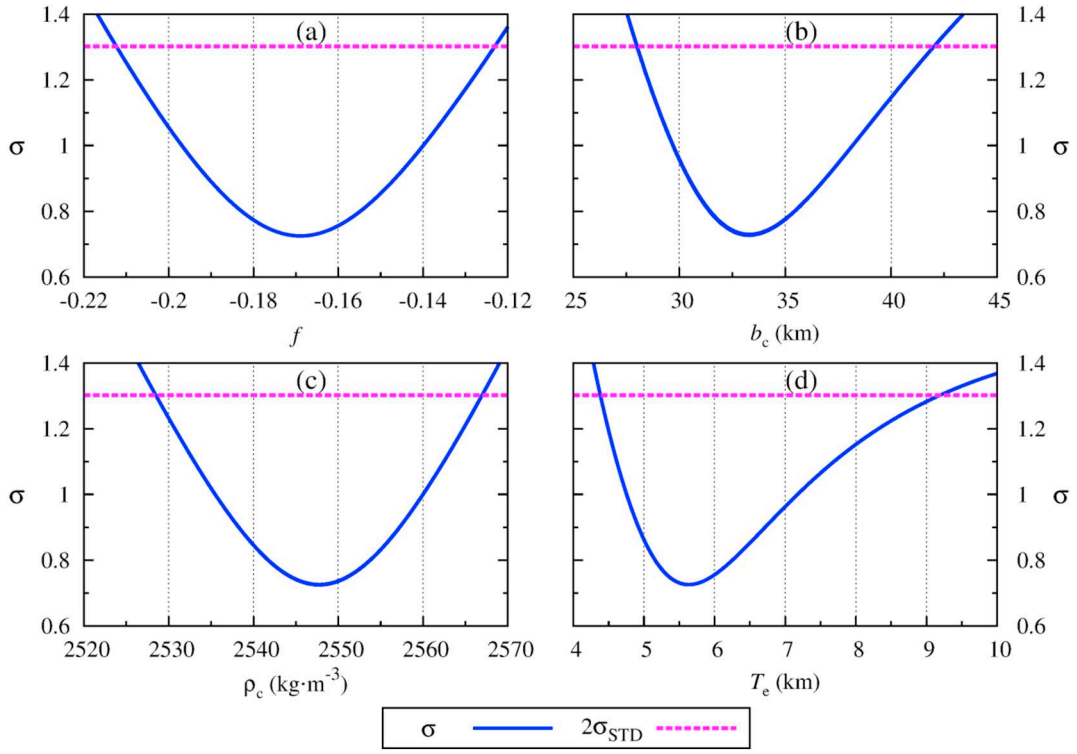

Fig. 7. Minimized misfits σ constrained within $2\sigma_{STD}$ for area No. 7 in Fig. 4 and in Table 2. Panels (a-d) are σ distributions concerning crustal density ρ_c, crustal thickness b_c, load ratio f and elastic thickness T_e, respectively.

7 are shown in Table 2, including load ratio f of -0.17, crustal thickness b_c of 33 km, crustal density ρ_c of 2550 kg·m^{-3} and elastic thickness T_e of 6 km.

We quantified the acceptable ranges of these parameters with the best-fit values. A trade-off study is shown in Fig. 6 for the area of No. 7. In Fig. 6a, the best-fit value of T_e was around 6 km with a corresponding f varying between -0.23 and -0.12. Such a best-fit value of T_e is also constrained in the rest panels with a range between 4 km and 12 km. Fig. 6b demonstrates that the best crustal thickness b_c ranges from 28 km to 42 km. The best crustal density in Fig. 6c lies between 2528 kg·m^{-3} and 2570 kg·m^{-3}. The exact ranges for these parameters are shown in Fig. 7. The best load ratio f in Fig. 7a is found to be $-0.17_{-0.042}^{+0.047}$, which includes the range shown in Fig. 6a. Such small load ratio indicates that the surface load is dominant rather than

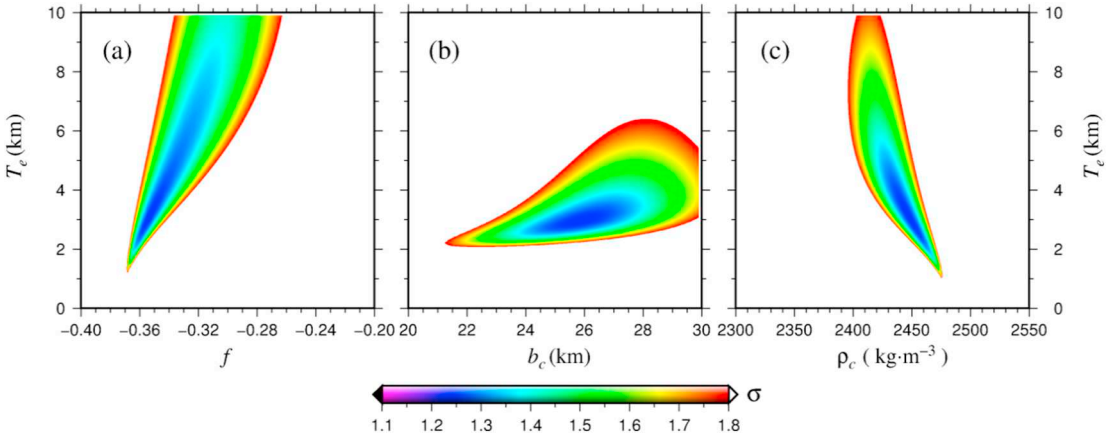

Fig. 8. RMS misfits σ in the trade-off studies between (a) f vs. T_e, (b) b_c vs. T_e and (b) ρ_c vs. T_e for area of No. 15 in Fig. 4 and in Table 2.

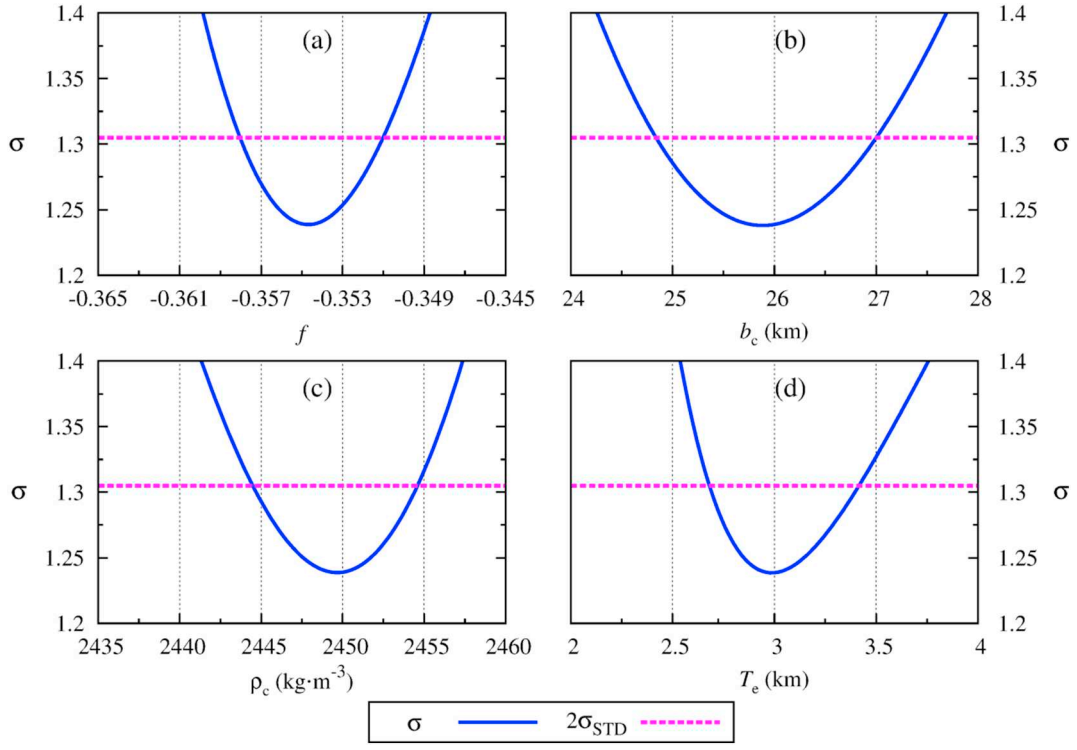

Fig. 9. Minimized misfits σ constrained within $2\sigma_{STD}$ for area No. 15 in Fig. 4 and in Table 2. Panels (a-d) are σ distributions concerning crustal density ρ_c, crustal thickness b_c, load ratio f and elastic thickness T_e, respectively.

the subsurface load, which is typical of highland or mountain regions. The range of best-fitting crustal thickness in Fig. 7b is coincident with that in Fig. 6b. The GRAIL gravity field model demonstrates that the crustal thickness of the whole highland has a minimum value of 34 km and a maximum value of 43 km (Wieczorek et al., 2013). Our estimated range for crustal thickness contains the likely mean value of the whole highland. The estimated value of crustal density is found to be 2550_{-22}^{+17} in Fig. 7c, which is roughly coincident with that range in Fig. 6c. This range involves the mean crustal density (~2550 kg·m^{-3}, Wieczorek et al., 2013) for the entire highland region. The elastic thickness in Fig. 7d varies between 4.39 km and 9.18 km. This range roughly approves those inFig. 6. Our results are reliable as they consider the best-constrained crustal thickness and crustal density.

We selected another area with the center at (55°S, 51°E) for our analysis (No. 15 in Table 2). In order to successfully estimate parameters within $2\sigma_{STD}$, we truncated the gravity and topography up to

170 (l_{max} = 170) and used a slightly larger angular radius of 6°, with a corresponding bandwidth of 43°. Fig. 8 shows the trade-offs between parameters, showing the narrow range of parameters, and quite different from those in Fig. 6. This is coincident with the large misfit σ (~1.2389) seen in Table 2. However, the parameters are constrained within $2\sigma_{STD}$ (~1.3203). Fig. 8a shows the range of f varying between −0.36 and −0.32. Fig. 8b gives a low crustal thickness with a range of [24 km, 27.5 km]. The constrained crustal density in Fig. 8c is around 2450 kg·m^{-3}. All the panels in Fig. 8 demonstrate that the elastic thickness is around 3 km. As to the range of load ratio, Fig. 9a shows a best-fit value around −0.355 while the crustal thickness ranges between 24.7 km and 27.1 km, and nearly coincident with the crustal thickness seen in Fig. 8b. Fig. 9c demonstrates a low crustal density range of [2444 kg·m^{-3}, 2455 kg·m^{-3}], which is substantially lower than the mean value of the entire highland (~2550 kg·m^{-3}). The best-fit value of elastic thickness in Fig. 9d is around 3 km, coincident with those in Fig. 8.

Using the same analysis, we find that not only does such small crustal density appear in the No. 7 and No. 15 areas, but also in other areas such as No. 5, 6, 8, 10, 11, 13, 14, 16, 17, 18, 19 and 20, as shown in Table 2. Although parts of these areas are not constrained within $2\sigma_{STD}$, the well constrained areas such as No. 6, 11, 15 and 20 demonstrate a lower crustal density than the mean crustal density value in the highland. Such small density, over areas 4 and 6 especially, coincides with the research of Wieczorek et al. (2013); but the density in the rest of areas approaches the surface density (Besserer et al., 2015). The recent work of Sori et al. (2018) demonstrates that the lunar highland topography formed early in lunar history before the development of a thick elastic lithosphere. Areas of No. 1 to 4 are nearby impact basins and the magma intrusion beneath these areas might increase the localized crustal density. The rest areas far away impact basins would sustain a relatively small density. The small crustal density is likely a result of high porosity of southern hemisphere highland. As to elastic thickness T_e, these slightly large values at No. 9 and No. 12 are not well constrained within $2\sigma_{STD}$ and do not represent the actual elastic thickness. Without considering No. 1, 2, 3, 4, 9 and 12, it can be concluded that the elastic thicknesses of the studied areas far from mare basins is around 7 km. The Feldspathic Highlands Terrane (FHT) consists of the central anorthositic region (FHT-An) and its outer region (FHT-O). The research of Kamata et al. (2013) implies that the lower crust underneath the FHT-O may be richer in radioactive elements than FHT-An. Recent research reported by Sori et al. (2018) implies that the farside highland (FHT-An) was formed earlier in lunar history before the development of a thick elastic lithosphere and was at large scale compensated by Airy mechanism. As part of the FHT, the southern highland was also likely formed before the development of a thick elastic lithosphere. Considering heating from the likely rich radioactive elements beneath the southern highland, a small elastic thickness is likely found there at the time of surface topography emplaced.

Areas No. 1 to No. 4 are close to Mare Humorum and Mare Nubium. The estimated parameters are well constrained over areas of No. 1 and No. 4. The area of No. 1 is beside Mare Humorum. The most precise estimated load ratio is around 3.448, and quite different from other places. Such large load ratio indicates that the subsurface load is dominant rather than the surface load. The best-fit value of the crustal density was around 2950 kg·m^{-3}. Such large load ratio and crustal density could be correlated with lava invading from Mare Humorum. The best-constrained elastic thickness is around 40 km. The large value of elastic thickness also appears in area of No. 4 (~30 km), shown in Fig. 4. This region is located on the south of Mare Nubium.

These relatively large thicknesses are distinct with the small values of the studied regions far from mare basins. The small elastic thicknesses (e.g. values at locations of No. 5-20) possibly correspond to the thicknesses at the stage of ancient surface topography formed after the solidification of Lunar Magma Ocean (LMO). After that, the lunar lithosphere developed quite thick as the lunar heat loss and becoming cooled of the Moon (Jolliff et al., 2006). Until impacting of mare basins' formation, the lunar lithosphere became greatly stiff to support mare loads. Melosh et al. (2013) verified that a strong lithosphere was essential to maintain a mascon. During the mare basin formation, the ejecta from impacts deposited throughout the edge of the basins and even mantle flow would intrude the subsurface structure beneath the surrounding of mare basins. The lithosphere elastically adjusted to support these new loads. A relatively large elastic thickness surrounding mare basin consequently developed. These large thicknesses were found in our studied regions such as No. 1 and No. 4, shown in Fig. 4.

5. Conclusion

In this paper, a strategy of self-adaptive inertia weight and a mutation operator are introduced in MPSO to estimate selenophysical parameters. Our results indicate that these strategies could help particles escape from localized minimization. A sensitivity analysis demonstrates that MPSO is more flexible in the choice of tuning parameters such as inertia weight ω, and cognitive and social parameters c_1 and c_2. A further test shows that a low mutation probability of 0.005 can promote convergence in global optima. A probability of 0.002 is used in parameters inversion. A particle swarm size of 400 and a maximum of 50 iterations are also employed and a best-fit is found between the modeled admittance spectrum and observations.

Using the updated MPSO algorithm, an extensive inversion on the lunar Southern Hemisphere highland is carried out. Parts of these areas are successfully constrained within two-standard deviation. Results indicate that a well-constrained crustal density for most of the studied regions is less than or equal to the mean crustal density (2550 kg·m^{-3}) of the entire lunar highland. The relatively small crustal density is likely a result of high porosity of crust on the southern hemisphere highland. The elastic thickness at studied locations far from mare basins is around 7 km, which is quite different with the large elastic thicknesses over locations nearby mare basins. Their difference potentially implies the distinct development stage of the lithosphere. The strength of the lithosphere was weak after the primordial topography formed from the crystallization of ancient ferroan anorthositic rock, thus a small elastic thickness can be found on the southern hemisphere highland. The ancient lunar lithosphere developed quite thick, as the loss of heat and becoming cool of the Moon. It was able to elastically support new loads during the formation of mare basins; hence a relatively large elastic thickness is likely found surrounding mare basins. The difference of elastic thickness indicates the development of lithospheric thickness at the distinct lunar evolutionary history.

Acknowledgements

The Generic mapping Tools (GMT) package was used to produce the figures in this paper. Our localized spherical harmonic analyses were performed using the freely available software archive SHTOOLS. This research is supported by Grant of the National Natural Science Foundation of China (41864001, U1831132), Open Fund of State Key Laboratory of Information Engineering in Surveying, Mapping and Remote Sensing, Wuhan University (Grant No. 17P03), and Guizhou Science and Technology Plan Project (Guizhou Science and Technology platform talents [2018]5769).

Appendix A. Flowchart of MPSO algorithm

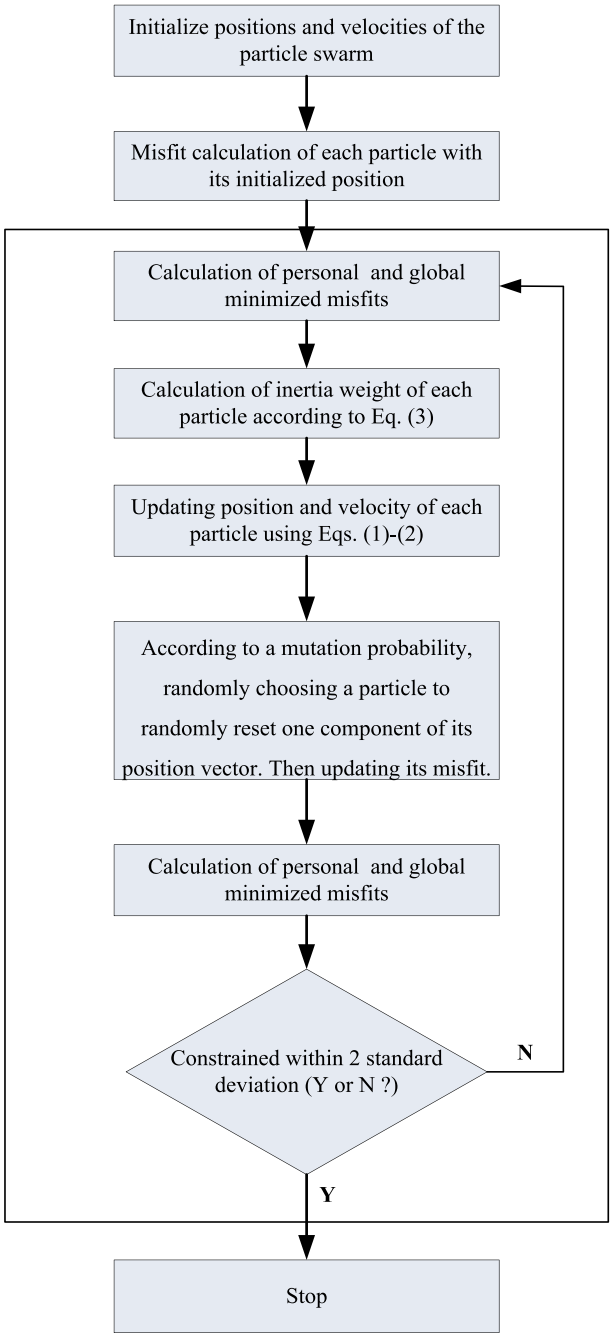

Fig. A1. Flowchart of MPSO.

Appendix B. Benchmark test functions

The n dimensional multimodal functions utilized to benchmark global optimization strategies are summarized in Table B1. Their application ranges, global minimum positions and values are illustrated as well. These functions can be used to evaluate characteristics of optimization algorithms, such as convergence rate and robustness. These tests are presented in Section 3, where the strategies of mutation and self-adaptive inertia weight were evaluated according to the success rate (SR). The SR is defined as the ratio between succeeding global-search times and the total number of tests. The larger the SR is, the robust the algorithm is. According to large value of SR, we can estimate the tuning parameters, such as self-adaptive inertia weight ω, cognitive and social factor c, and mutation probability p_m. In this paper, we take the dimension $n = 2$ for simplification.

Table B1
Benchmark test functions, where x_i is the i-th component of the position.

Function	Formula	Range	Solution	Global Minimum
Ackley	$-20e^{-0.2\sqrt{\frac{\sum_{i=1}^{n} x_i^2}{n}}} - e^{\frac{\sum_{i=1}^{n}\cos(2\pi x_i)}{n}} + 20 + e$	$[-32, 32]$	$(0)^n$	0
Rastrigin	$10n + \sum_{i=1}^{n}[x_i^2 - 10\cos(2\pi x_i)]$	$[-5.12, 5.12]$	$(0)^n$	0

Appendix C. Lithospherical deflections corresponding to various loads

Not only surface load does cause the deflection of the lithosphere, but also subsurface load (Forsyth, 1985). Assuming the initial amplitudes of the surface and subsurface loads are h_i and w_i, respectively, and h_t and w_b are their heights after loading, it can be deduced their corresponding lithospherical deflection w_t and h_b (Forsyth, 1985)

$$h_i = h_t + w_t \tag{C1}$$

$$w_i = w_b + h_b \tag{C2}$$

Accordingly, the observed surface topography h and subsurface load interface w represent a sum of the components:

$$h = h_t - h_b \tag{C3}$$

$$w = w_b - w_t \tag{C4}$$

The actual lithosphere deflection is possibly produced by the combination of the surface and subsurface loads. We here introduced a model involving four interfaces, which is shown in Table C1. The quantities of b_c and z_b represents the crustal thickness and subsurface load depth, respectively. Supposing subsurface load generates at the crust-mantle interface, we can have the relationship $b_c = z_b$. Accordingly, the load generated by the combination of surface and subsurface loads is

$$q = g[\rho_c h - (\rho_m - \rho_c)(h_b + w_t) + \rho_b(w_b - w_t) + \rho_b(h_b + w_t)] \tag{C5}$$

where ρ_b is the density contrast between the subsurface load and its surroundings. In order to solve Eq. (10) according to observed topography h, Forsyth (1985) introduced load-ratio f and it defined as

$$f = \frac{\rho_b w_i}{\rho_c h_i} \tag{C6}$$

Considering Eqs. (C1)–(C6), the actual deflection w_L of the lithosphere is

$$w_L = -k_1 \cdot h - k_2 \cdot w \tag{C7}$$

where

$$k_1 = \frac{f\rho_c}{f\rho_c + \rho_m - \rho_c} \tag{C8}$$

$$k_2 = \frac{\rho_m - \rho_c}{f\rho_c + \rho_m - \rho_c} \tag{C9}$$

Eq. (10) is clearly a nonlinear equation and it is impossible to deduce its exact solution. However, it is still solved as spherical harmonic form when assuming the estimated parameters being isotropic (Beuthe et al., 2012). Considering isotropic estimated parameters, the spherical harmonic coefficient w_{lm} of subsurface load interface w can be expressed as

$$w_{lm} = -\frac{k_3(l)}{k_4(l)} h_{lm} \tag{C10}$$

where

$$k_3(l) = \sigma k_1 \cdot \lambda_1(l) + \tau k_1 \cdot \lambda_2(l) + \frac{\rho_c}{\rho_m - \rho_c}\lambda_3(l) \tag{C11}$$

$$k_4(l) = \sigma k_2 \cdot \lambda_1(l) + \tau k_2 \cdot \lambda_2(l) + \lambda_3(l) \tag{C12}$$

$$\lambda_1(l) = l^3(l+1)^3 - 4l^2(l+1)^2 \tag{C13}$$

$$\lambda_2(l) = l(l+1) - 2 \tag{C14}$$

$$\lambda_3(l) = l(l+1) - 1 + v \tag{C15}$$

$$\sigma = \frac{D}{gR^4(\rho_m - \rho_c)} \tag{C16}$$

$$\tau = \frac{\mathrm{E}T_e R^2}{\mathrm{gR}^4(\rho_m - \rho_c)} \quad \text{(C17)}$$

where h_{lm} is the spherical harmonic coefficient with degree l and order m of the observed topography h. Given a serial of estimated parameters such as f, b_c, ρ_c and T_e, it can be estimated the resulted amplitudes of interfaces in Table C1 as well as the corresponding surface gravity anomaly.

Table C1
The referenced interfaces employed in modeled gravity anomaly calculation.

No.	Interface	Height of Interface	Density contrast	Referenced radius
1	Surface	H	ρ_c	R
2	Crust-Mantle interface	$-(h_b + w_t)$	ρ_m-ρ_c	R-b_c
3	Subsurface load	w_b-w_t	ρ_b	R-z_b
4	Reference layer of Subsurface load	$-(h_b + w_t)$	$-\rho_b$	R-z_b

References

Ali, R., Mounir, G., Moncef, T., 2016. Adaptive probabilities of crossover and mutation in genetic algorithm for solving stochastic vehicle routing problem. International Journal of Advanced Intelligence Paradigms 8 (3), 318.

Arkani-Hamed, J., 1998. The lunar mascons revisited. J. Geophy. Res. 103 (E2), 3709–3739.

Belleguic, V., Lognonne, P., Wieczorek, M.A., 2005. Constraints on the Martian lithosphere from gravity and topography data. J. Geophys. Res. 110, 1–22.

Bendat, J.S., Piersol, A.G., 2000. Random data: analysis and measurement procedures. John Wiley, New York.

Besserer, J., Nimmo, F., Wieczorek, M.A., et al., 2015. GRAIL gravity constraints on the vertical and lateral density structure of the lunar crust. Geophy. Res. Lett. 41 (16), 5771–5777.

Beuthe, M., Maistre, L., Rosenblatt, P., et al., 2012. Density and lithospheric thickness of the Tharsis Province from MEX MaRS and MRO gravity data. J. Geophy. Res. 117 (E04002), 1–32.

Chenet, H., Ph, Lognonne, Wieczorek, M., et al., 2006. Lateral variations of lunar crustal thickness from the Apollo seismic data set. Earth Planet. Sci. Lett. 243 (1), 1–14.

Crosby, A., McKenzie, D., 2005. Measurements of the elastic thickness under ancient lunar terrain. ICARUS 173 (1), 100–107.

Dai, C.H., Zhu, Y.F., Chen, W.R., 2006. Adaptive probabilities of crossover and mutation in genetic algorithms based on cloud model. IEEE Information Theory Workshop. 24 (4), 710–713.

Forsyth, D.W., 1985. Subsurface loading and estimates of the flexural rigidity of continental lithosphere. J. Geophys. Res. 90, 12623–12632.

Garcia, R.F., Gagnepain-Beyneix, J., 2011. Chevrot S, et al. Very preliminary reference Moon model. Phys. Earth Planet. Inter 188 (1–2), 96–113.

Gillet, K., Margerin, L., Calvet, M., et al., 2017. Scattering attenuation profile of the moon: implications for shallow moonquakes and the structure of the megaregolith. Phys. Earth Planet. Inter. 262, 28–40.

Goossens, S., Matsumoto, K., Liu, Q., et al., 2011. Lunar gravity field determination using SELENE same-beam differential VLBI tracking data. J. Geod. 85 (4), 205–228.

Huang, Q., Wieczorek, M.A., 2012. Density and porosity of the lunar crust from gravity and topography. J. Geophy. Res. 117 (E05003), 1–9.

Huang, Q., Xiao, Z.Y., Xiao, L., 2014. Subsurface structures of large volcanic complexes on the nearside of the moon: a view from GRAILL gravity. Icarus 243, 48–57.

Ishihara, Y., Namiki, N., Sugita, S., et al., 2009. Localized gravity/topography correlation and admittance spectra one the Moon, No. 1623. In: 40th Lunar and Planetary Science Conference.

Jin, S.G., Arivazhagan, S., Araki, H., 2013. New results and questions of lunar exploration from SELENE, Chang'E-1, Chandrayaan-1 and LRO/LCROSS. Adv. Space Res. 52 (2), 285–305.

Jolliff B L, Wieczorek, M A, Shearer, Shearer C K and Neal C R (Eds.). 2006. New views of the Moon (Vol. 60). Walter de Gruyter GmbH & Co KG.

Kamata, S., Sugita, S., Abe, Y., et al., 2013. Viscoelastic deformation of lunar impact basin: implications for heterogeneity in the deep crustal paleo-thermal state and radioactive element concentration. J. Geophy. Res. 118 (3), 398–415.

Kennedy J and Eberhart R. Particle swarm optimization. 1995. In proceedings of ICNN'95 – International Conference on Neural Networks, volume 4, pages 1942-1948. IEEE, ISBN 0-7803-2768-3.

Kennedy, J., Eberhart, R.C., Shi, Y., 2001. Swarm Intelligence. 291 Morgan Kaufmann, San Francisco.

Khan, A., Mosegaard, K., Rasmussen, K.L., 2000. A new seismic velocity model for the moon from a Monte Carlo inversion of the Apollo lunar seismic data. Geophy. Res. Lett. 27 (11), 1591–1594.

Kohlstedt, D.L., Evans, B., Mackwell, S.J., 1995. Strength of the lithosphere: constraints imposed by laboratory experiments. J. Geophy. Res. 100 (B9), 17587–17602.

Konopliv, A.S., Park, R.S., Yuan, D.N., et al., 2013. The JPL lunar gravity field to spherical harmonic degree 660 from the GRALL Primary Mission. J. Geophy. Res. 118, 1415–1434.

Kraus H. 1967. Thin Elastic Shell: An Introduction to the Theoretical Foundations and the Analysis of Their Static and Dynamic Behavior. John Wiley, Hoboken N J, 467 PP.,

Latham G, Ewing M, Dorman J, et al. 1973. Lunar structure and dynamics-results from the apollo passive seismic experiment. Moon, 7(3–4):396–421.

Matsumoto, K., Goossens, S., Ishihara, Y., et al., 2010. An improved lunar gravity field model from SELENE and historical tracking data: revealing the farside gravity features. J. Geophy. Res. 115 (E06007), 258–273.

Matsumoto, K., Yamada, R., Kikuchi, F., et al., 2015. Internal structure of the moon inferred from Apollo seismic data and selenodetic data from GRAIL and LLR. Geophys. Res. Lett. 42 (18), 7351–7358.

McGovern, P.J., Solomon, S.C., Smith, D.E., et al., 2002. Localized gravity/topography admittance and correlation spectra on Mars: implications for regional and global evolution. J. Geophy. Res. 107, 1–19.

Melosh, H.J., Freed, A.M., Johnson, B.C., et al., 2013. The origin of lunar mascon basins. Science 340 (6140), 1552–1555.

Nakamura, Y., Lammlein, D., Latham, G., et al., 1973. New seismic data on the state of the deep lunar interior. Science 181 (4094), 49–51.

Namiki, N., 2010. Admittance and correlation of localized gravity and topography of Freundlich-Sharonov basin of the Moon. In: 1885, 41st Lunar and Planetary Science Conference.

Shi, Y., Eberhart, R., 1998. A modified particle swarm optimizer. In: Proceedings of the IEEE International Conference on Evolutionary Computation, pp. 69–73.

Smith, D.E., Zuber, M.T., Neumann, G.A., et al., 2010. Initial observation from the Lunar Orbiter Laser Altimeter (LOLA). Geophys. Res. Lett. 37, 1–6.

Sori, M.M., James, P.B., Johnson, B.C., et al., 2018. Isostatic compensation of the lunar highlands. J. Geophy. Res. Planet. https://doi.org/10.1002/2017JE005362.

Sugano, T., Heki, K., 2004. Isostasy of the Moon from high-resolution gravity and topography data: implication for its thermal history. Geophy. Res. Lett. 31 (24), 1183–1186.

Taherkhani, M., Safabakhsh, R., 2016. A novel stability-based adaptive inertia weight for particle swarm optimization. Appl. Soft Comput. 38, 281–295.

Turcotte, D.L., Fm, Haxby W., Norberry, J., 1981. Role of membrane stresses in the support of planetary topography. Sc. Lett. 324, 269–279.

Watts, A.B., 1994. Crustal structure, gravity anomalies and flexure of the lithosphere in the vicinity of the Canary Islands. Geophys. J. Int. 119 (2), 648–666.

Wieczorek, M.A., Meschede, M., 2018. SHTools-tools for working with spherical harmonics. Geochem. Geophys. Geosyst. https://doi.org/10.1029/2018GC007529.

Wieczorek, M.A., Simons, F.J., 2005. Localized spectral analysis on the sphere. Geophy. J. Int. 162, 655–675.

Wieczorek, M.A., Simons, F.J., 2007. Minimum-variance multitaper spectral estimation on the sphere. J. Fourier Anal. Appl. 13, 665–692.

Wieczorek, M.A., Neumann, G.A., Nimmo, F., et al., 2013. The crust of the moon as seen by GRAIL. Science 339, 671–675.

Zhong, S. j, Zuber, M.T., 2002. Long-wavelength topographic relaxation for self-gravitating planets and implications for the time-dependent compensation of surface topography. J. Geophy. Res. 105, 4153–4164.

Zhong, Z., Li, F., Yan, J., et al., 2014. Lunar geophysical parameters inversion based on gravity/topography admittance and particle swarm optimization. Adv. Space Res. 54, 770–779.

Zhong, Z., Jianguo, Y., Rodriguez, J., Alexis, P., James, D., 2017. Ancient selenophysical structure of the Grimaldi basin: constraints from GRAIL gravity and LOLA topography. Icarus 309, 411–421.

Zuber, M.T., Smith, D.E., Watkins, M.M., et al., 2013. Gravity Field of the Moon from the Gravity Recovery and Interior Laboratory (GRAIL) Mission. Science 339, 668–671.